

Lateral bearing factors and elastic stiffness factors for robotic CPT p-y module in undrained clay

Kai Wen^{a,*}, Benjamin Cerfontaine^a, David White^a, Susan Gourvenec^a, Andrea Diambra^b

^a Department of Civil, Maritime and Environmental Engineering, University of Southampton, Southampton SO16 7QF, UK

^b Department of Civil Engineering, University of Bristol, Bristol BS8 1TR, UK

ARTICLE INFO

Keywords:

ROBOCONE p-y module
Undrained clay
Upper bound analysis
Finite element simulation
Lateral bearing factor
Elastic stiffness factor

ABSTRACT

There is a strong incentive to enhance in-situ ground characterisation tools to provide additional data that supports early infrastructure design in engineering projects, prior to completion of laboratory element testing on borehole samples. Advances in robotic technology allow additional soil deformation modes to be probed by integrating a cylindrical section of cone capable of horizontal translation into an expanded standard cone penetrometer, referred to here as ROBOCONE p-y module, which can mimic the load and displacement behaviour of laterally loaded pile element. This paper presents a series of three-dimensional elasto-plastic finite element simulations and semi-analytical upper bound analyses of this p-y module in homogeneous, undrained clay. The aim is to support the optimal choice of p-y module geometry and to lay the foundation of an interpretation method. In particular, the paper investigates the lateral bearing factor (N_{RC}) and elastic stiffness factor (K_{RC}) required for the measured load–displacement curves to be converted into practical design soil parameters such as undrained shear strength and elastic shear modulus. The numerical results reveal that N_{RC} varies inversely with the height-diameter ratio (H_R/D_R) of the p-y module and interface roughness, and these factors are compared to semi-analytical upper-bound solutions. Correction factors that allow for the finite length of the p-y module are derived, and these have minimal variation with interface roughness. The height-diameter ratio H_R/D_R has a similar influence on K_{RC} . Simple mechanism-based expressions for the lateral bearing and stiffness factors are devised to generalize the numerical results and provide definitive solutions to determine soil undrained strength and elastic stiffness from ROBOCONE p-y module measurements.

1. Introduction

Throughout geotechnical engineering there is an impetus to improve the data that can be gathered from in situ tests, because (i) these tests are performed early in the site investigation programme, and so are available to designers prior to laboratory testing of samples, and (ii) in situ tests are unaffected by the soil disturbance associated with sampling and lab testing. For example, to achieve the UK's 2050 net-zero emission target, a substantial growth in the volume of offshore site surveys is required to support the expansion of offshore renewable energy (Cerfontaine et al., 2023). To accelerate this development, more efficient site characterisation tools are needed to reduce the number of lab tests that must be undertaken onshore, which are currently saturating the available laboratory facilities and exploration vessels.

The prevalent design methodology for laterally loaded piles involves

the utilization of non-linear lateral load–displacement (p-y) springs, wherein the stiffness and resistances are conventionally linked to soil strength and stiffness parameters, or to CPT tip resistance (Matlock, 1970; Byrne et al., 2020; Jeanjean et al., 2022; White et al., 2022). A variety of advanced site investigation tools including pressuremeters, flow-round penetrometers and flat dilatometers also exist (Houlsby and Carter, 1993; Randolph et al., 1998; Yan et al., 2011; Truong & Lehane, 2014), but have not yet found wide adoption, partly due to the equipment complexity but also because of the lack of robust methods to convert their measurements into soil parameters. In situ tests can be most easily applied to design if they involve loading and soil deformation that closely matches the design scenario – as is the case, for example, when scaling from CPT tip resistance to pile base capacity. This has led to initiatives to expand the CPT to include additional aspects that more faithfully replicate the loading conditions of infrastructure

* Corresponding author.

E-mail addresses: k.wen@soton.ac.uk (K. Wen), b.cerfontaine@soton.ac.uk (B. Cerfontaine), david.white@soton.ac.uk (D. White), susan.gourvenec@soton.ac.uk (S. Gourvenec), Andrea.Diambra@bristol.ac.uk (A. Diambra).

<https://doi.org/10.1016/j.compgeo.2024.106487>

Received 20 February 2024; Received in revised form 24 May 2024; Accepted 29 May 2024

Available online 4 June 2024

0266-352X/© 2024 The Author(s). Published by Elsevier Ltd. This is an open access article under the CC BY license (<http://creativecommons.org/licenses/by/4.0/>).

throughout their service life (White, 2022). These include the use of new robotic and sensing techniques such as implementation of a series of friction sleeves with torsional load and axial load sensing capabilities in the standard CPT (Martinez & Frost, 2018).

A further advance in this direction is integrating a short cylindrical section capable of actuating laterally into the conventional CPT – referred to as a p-y module, as shown in Fig. 1 (Diambra et al., 2022; Creasey et al., 2023). The p-y module, with a diameter of D_R and a length of H_R , mimics the load and displacement history imposed by a laterally loaded pile element, enabling the direct measurements of nonlinear lateral load–displacement soil springs akin to those used in the design of laterally loaded piles (Bateman et al., 2023). While the measured response can be converted into soil properties, including undrained shear strength and elastic shear modulus, there exists a need of robust methodology equivalent to the bearing and stiffness factor successfully developed for existing penetrometer tests (e.g. Teh and Housby, 1991, Yan et al., 2011).

To develop such solutions for the ROBOCONE p-y module, in this study finite element (FE) approach has been adopted, following the approach used for interpretation of other in-situ ground characterisation tools (Yu et al., 2005; Moavenian et al., 2016; Liu et al., 2019; Charles et al., 2020). For example, Housby and Carter (1993) carried out analyses of undrained pressuremeter tests, and demonstrated how the derived pressure-expansion curves can be converted into shear modulus and undrained shear strength allowing for corrections due to the finite length-diameter ratio of a pressuremeter. Similarly, Yan et al. (2011) and Stanier & White (2015) presented systematic studies of the shallowly embedded hemispherical and toroidal penetrometers to develop scaling factors from the measured load–displacement data to undrained strength and shear stiffness. Since the ROBOCONE p-y module is a new test concept, no finite element simulations have so far been conducted to aid in the interpretation of this type of soil probing.

The goal of this paper is to develop an interpretation framework of bearing and stiffness factors for the ROBOCONE p-y module to allow the undrained strength and elastic stiffness properties of the soil to be determined from monotonic load–displacement measurements. To this end, finite-element analyses of a ROBOCONE p-y module in undrained

soils were undertaken for a range of geometries. These analyses also provide insights to support optimisation of the p-y module’s geometry as well as the best procedures for its deployment. An semi-analytical upper bound analysis, validated against the finite element analysis, serves as the foundation of the interpretation framework.

2. Semi-analytical upper-bound analyses

Semi-analytical upper bound limit analyses are first developed in this section for the p-y module in undrained clay, making use of a postulated soil failure mechanism and equating the rate of energy dissipation within the deforming soil mass to the work done by the resistance of p-y module. These upper bound solutions are characterised by their simplicity and straightforwardness and serve as a benchmark for the subsequent finite element simulations, particularly in terms of bearing factors.

The upper bound analysis for the p-y module extends the soil failure mechanism in plane strain conditions initially developed for a circular infinitely long rigid pile with radius R (Martin & Randolph, 2006). This plane strain mechanism, referred to as the ‘rigid crescent’ mechanism hereafter, assumes a crescent-shaped block of soil undergoing rigid body rotation about a point on the transverse axis of pile. As required by plasticity limit analysis, the soil is assumed to be an incompressible perfectly plastic material with undrained shear strength s_u , while the pile-soil interface strength is characterised by a constant value αs_u (where α is the interface roughness ranging from 0.0 to 1.0). The location of the centre of soil rotation, at a distance of λR from the pile centre, is treated as a variable that can be optimised freely to achieve a minimal bearing factor, N . As a result, the upper bound solution can be expressed as a function of λ and α , as given by Equation (1).

$$N = \frac{(1 + \lambda^2)(\pi + 2\lambda \tan^{-1} \lambda) + \alpha \pi}{\lambda} \quad (1)$$

As noted in Martin & Randolph (2006), Equation (1) deduced from the rigid crescent mechanism is able to provide improved bearing factors relative to the upper-bound solution of Randolph & Housby (1984) for

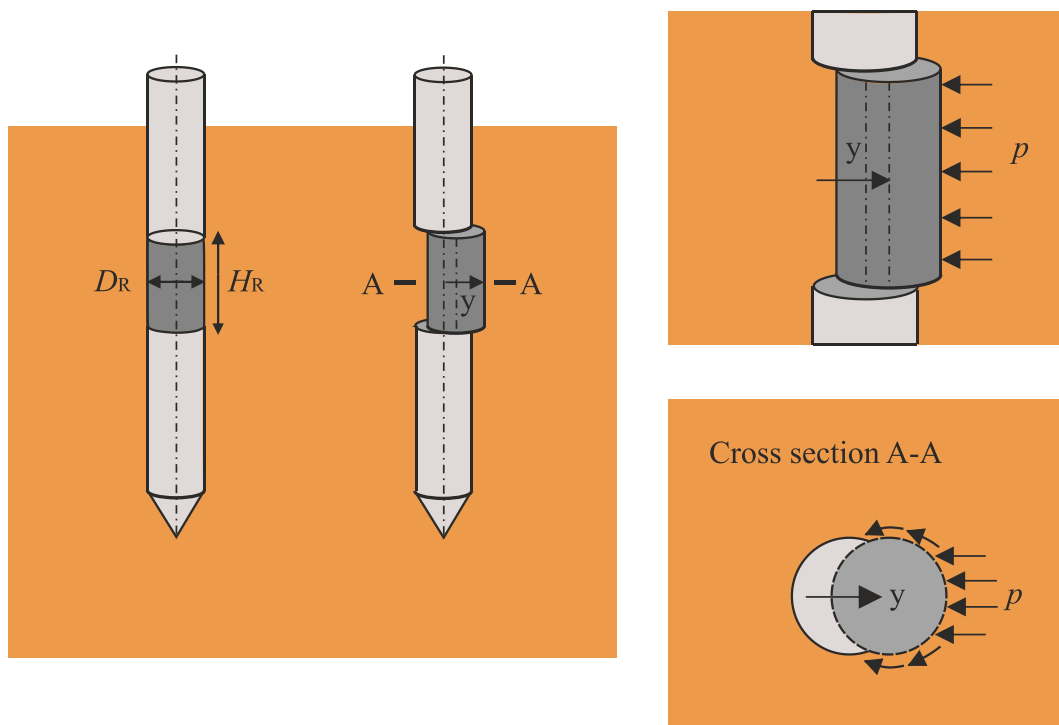


Fig. 1. Illustration of the ROBOCONE p-y module and its working mechanism (adapted from Diambra et al., 2022)

small values of $\alpha < 0.5$, as it considerably reduces the discrepancy with respect to the closed form lower-bound solution of [Randolph & Houlsby \(1984\)](#). [Martin & Randolph \(2006\)](#) describes another soil mechanism that is a combination of the innermost rigid crescent block and the surrounded zones of shearing, referred to as ‘combined mechanism’ hereafter, which demonstrates excellent accuracy across all values of α . However, this study mainly focused on the simpler rigid crescent mechanism and extended it to the three-dimensional version for the analysis of ROBOCONE p-y module.

[Fig. 2\(a\)](#) shows the three-dimensional soil failure mechanism around a ROBOCONE p-y module (with a radius R) moving with a velocity v_0 in the x-direction. The failure soil is bounded by the top and bottom horizontal surfaces (referred to here as ‘end planes’), along which planar shearing occurs, with the soil above the top end plane and below the bottom end plane remaining stationary. The deformed soil volume was discretized into a series of flowing channels rotating about the vertical axis at $(0, \lambda R, 0)$, as seen in [Fig. 2\(a\)](#). To carry out the upper bound calculation for determining the bearing factor of the ROBOCONE p-y module (N_{RC}), it is useful to consider the shaft component and end components separately, as expressed by:

$$N_{RC} = \frac{F_{t,RC}}{D_R H_R s_u} = \frac{F_{s,RC} + F_{e,RC}}{D_R H_R s_u} = N_{s,RC} + N_{e,RC} \left(\frac{D_R}{H_R} \right) \quad (2)$$

$$N_{s,RC} = \frac{F_{s,RC}}{D_R H_R s_u} \quad (3)$$

$$N_{e,RC} = \frac{F_{e,RC}}{D_R^2 s_u} \quad (4)$$

Where $F_{t,RC}$ is the total reaction force measured directly by p-y module equipment that can be split into the contributions by the shaft and two end planes of the soil volume displaced (referred to as $F_{s,RC}$ and $F_{e,RC}$ respectively hereafter); D_R and H_R are the diameter and height of a p-y module, respectively. $N_{s,RC}$ is the shaft bearing factor that can be directly determined from Equation (1), while $N_{e,RC}$ is the end bearing factor to be derived in this study.

[Fig. 2\(b\)](#) shows the top end plane of the displaced soil volume and the associated velocity field of various stripes rotating about the centre $Y(0, \lambda R)$. Following the upper bound methodology, the end bearing capacity of p-y module ($F_{e,RC}$, see Equation (3)) can be determined by equating its work done to the energy dissipation across all the shearing stripes over the end plane, as given by:

$$F_{e,RC} \cdot v_0 = 2 \cdot 4s_u \int v(i) \cdot A(i) di \quad (5)$$

Where $v(i)$ and $A(i)$ are the average velocity and area of the i -th shearing stripes respectively. The factor of 4 represents the complete end plane, as only a quarter of the mechanism is represented in [Fig. 2b](#). The factor of 2 stands for the contribution from both the top and bottom end planes.

Considering the i -th soil shearing stripe $X_i X_{i+1} X'_i X'_{i+1}$ (coloured in cyan), the coordinates of the point X_i on the circumference is given by $(R \cos \psi_i, R \sin \psi_i)$. Meanwhile, the associated angle θ_i formed by lines YO and $X_i Y$ can be expressed as a function of ψ_i :

$$\theta_i = \sin^{-1} \left(\frac{\cos \psi_i}{\sqrt{1 + \lambda^2 - 2\lambda \sin \psi_i}} \right) \text{ When } \psi_i \leq \sin^{-1} \lambda \quad (6)$$

$$\theta_i = \pi - \sin^{-1} \left(\frac{\cos \psi_i}{\sqrt{1 + \lambda^2 - 2\lambda \sin \psi_i}} \right) \text{ When } \psi_i > \sin^{-1} \lambda \quad (7)$$

The soil velocity at the point X_i on the circumference (v_{X_i}) is a product of angular velocity $\omega = v_0 / \lambda R$ and the length of $X_i Y$, as given by:

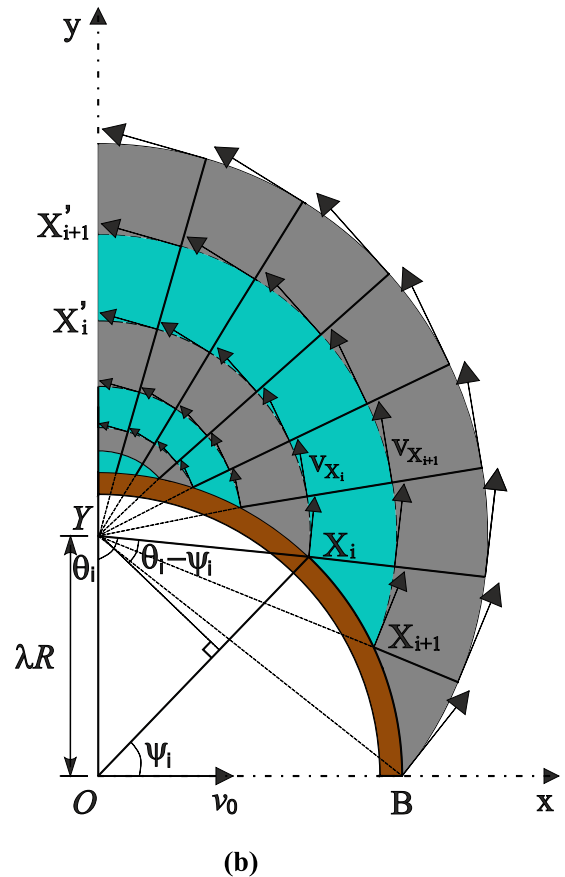
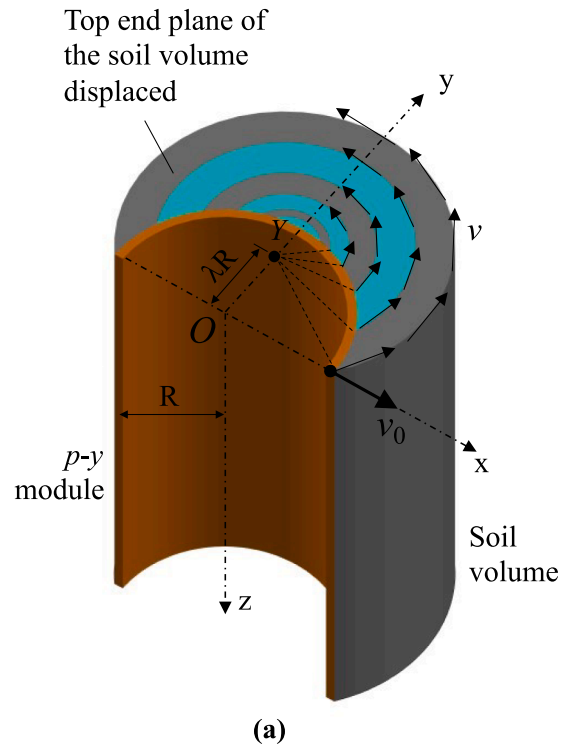


Fig. 2. (a) Three-dimensional soil failure mechanism around a p-y module moving laterally along axis x; (b) postulated soil failure mechanism at the end plane of the displaced soil volume (adapted from [Martin and Randolph, 2006](#))

$$|v_{X_i}| = \omega \bullet X_i Y = \frac{v_0}{\lambda R} \bullet \frac{\lambda R \cos \psi_i}{\cos(\theta_i - \psi_i)} = \frac{v_0 \cos \psi_i}{\cos(\theta_i - \psi_i)} \quad (8)$$

The average velocity across this shearing stripe is approximately calculated by:

$$v(i) = \frac{v_{X_i} + v_{X_{i+1}}}{2} \quad (9)$$

The width of this shearing stripe has magnitude:

$$W(i) = X_{i+1} Y - X_i Y \quad (10)$$

The average length of this shearing stripe is given by:

$$L(i) = \frac{X_{i+1} X'_{i+1} + X_i X'_i}{2} = \frac{X_i Y \bullet (\pi - \theta_i) + X_{i+1} Y \bullet (\pi - \theta_i)}{2} \quad (11)$$

The area of this shearing stripe is given by:

$$A(i) = W(i) \bullet L(i) \quad (12)$$

Substituting the Equations (4–12) into Equation (3) can yield the expression for the end bearing factor $N_{e,RC}$ as:

$$N_{e,RC} = \frac{F_{e,RC}}{s_u D_R^2} = \frac{8 \int v(i) \bullet A(i) di}{v_0 \bullet D_R^2} \quad (13)$$

The Equation (13) allows to calculate the $N_{e,RC}$ through numerical integration, recognising that it is unlikely to produce an explicit expression. In this case, λ is treated as a variable that can be optimised freely to achieve the minimum of $N_{e,RC}$ for a particular interface roughness factor (α). Note that the total bearing factor ($N_{e,RC}$) is independent of the p-y module's moving velocity v_0 .

Fig. 3 (a) shows a family of optimum λ values obtained for various aspect ratios ($1.0 < H_R/D_R < \infty$) and interface roughness ($0.0 < \alpha < 1.0$). As noted earlier, the λ , from a physical perspective, is relevant to the size of soil volume that was in plastic failure due to the horizontal translation of p-y module (see Fig. 2). At a specific interface roughness factor, λ is found to increase with the aspect ratio, indicating a bigger failure envelope area for longer p-y module and vice versa, as illustrated in Fig. 3 (b). Furthermore, at a specific aspect ratio of p-y module, the failure envelope expands as the interface roughness increases, aligning with observations made by Martin & Randolph (2006). Fig. 3 (c) shows the enhancement of total bearing factors with the increase in both interface roughness and aspect ratios. Taking advantage of Equation (2), it can be inferred that the end bearing factors ($N_{e,RC}$) are approximately 34% of the shaft bearing factor ($N_{s,RC}$), with slight fluctuation associated with the interface roughness.

3. Finite element model

The finite element analyses presented in this study were carried out with the commercial software PLAXIS 3D V23 (PLAXIS, 2023). Taking advantage of the double symmetry of p-y module geometry, only a quadrant of model was simulated to reduce the computational cost while maintaining accuracy. Fig. 4 illustrates the layout of the ROBOCONE system (including shaft, rings and moveable p-y module) embedded in the soil domain. The CPT shaft had an external diameter of 54 mm and a wall thickness of 2 mm, following the specification of the prototype p-y module (Creasey et al., 2023), although all results are presented in a normalised form to be applicable to any scale of device. The height (H_R) of the p-y module was treated as a key variable whose influence on the p-y module response is to be investigated systematically. Note that five moveable rings were modelled between the p-y module and the fixed shaft above, with dimensions that match the rings on the prototype device. These rings also allow to minimise the mesh distortion near the top of p-y module during lateral movement.

A cylindrical soil domain, with a thickness of 0.5 m and a diameter of

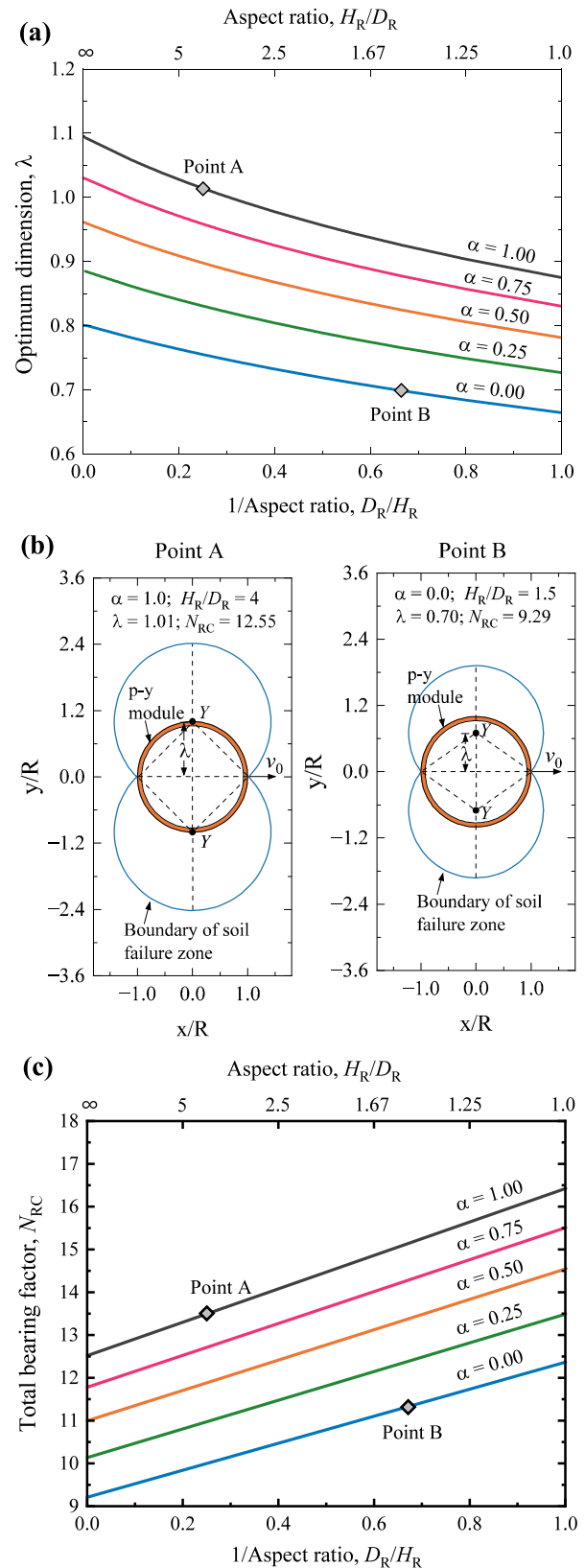


Fig. 3. (a) Optimum λ as a function of aspect ratio (H_R/D_R) and interface roughness (α); (b) normalised failure envelop around p-y module with two representative conditions; (c) semi-analytical bearing factor as a function of aspect ratio and interface roughness.

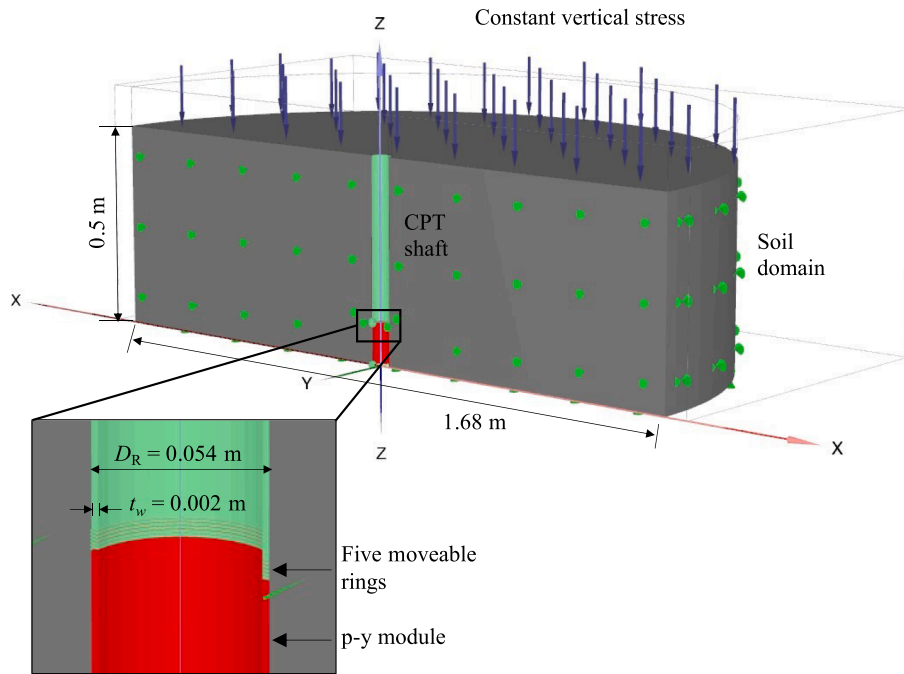


Fig. 4. The geometry and boundary conditions for ROBOCONE device in undrained soils.

1.68 m (approximately $30D_R$), was specified to avoid any boundary effects on the response of p-y module, based on prior analyses that assessed this effect. Horizontal radial fixity in directions X and Y (Fig. 4) was applied at the boundary, while the symmetry planes ($Y_{\min} = 0$ and $Z_{\min} = 0$) were normally fixed to prevent orthogonal movements.

The soil domain was discretised by a range of second-order tetrahedral elements, each with 10-nodes and four Gaussian integration points. A finer discretisation was designated close to the p-y module where stress concentrations are found and to minimise the mesh dependency of FE results. The ROBOCONE system (including shaft, a stack of rings and moveable p-y module) was treated as a rigid body with six degrees of freedoms to be imposed or fixed, with the number of elements varying based on the p-y module geometry. The soil-structure interaction was modelled using “zero-thickness” interface elements.

The soil was modelled as a weightless, homogeneous, undrained material, using linear isotropic elasticity and a Tresca failure criterion for plasticity. An associated flow rule was assumed. Consequently, the soil was characterised in terms of shear modulus (G) and undrained shear strength (s_u). A tension cut-off option was specified for the clay, with zero tensile strength, although the confinement around the ROBOCONE prevented any gaps opening up at the failure load. While this constitutive model simplifies undrained soil behaviour and does not capture the sensitivity of the shear modulus to strain levels, it is sufficient to study the elastoplastic behaviour of the p-y module to find initial stiffness and ultimate bearing factors, following the same approach used for other devices such as the pressuremeter (Houlsby and Carter, 1993). Two constant values of s_u ($=30$ kPa) and G ($=4.6$ MPa) were specified in the subsequent FE analyses. Since bearing and stiffness factors in this study were both calculated from forces normalised with respect to s_u and G , the FE results are independent of the choice of a specific value.

The mechanical behaviour of the interface elements for soil-structure interaction was modelled using the linearly elastic-perfectly plastic model, for which the maximum shear strength is defined as αs_u , with $0 < \alpha \leq 1.0$. The interface normal and shear stiffness were initially specified as $K_{s,i} = 4.7 \times 10^5$ kN/m³, $K_{n,i} = 5.17 \times 10^6$ kN/m³ respectively, to avoid numerical issues created by low stiffness associated with the automatic calculation of K_s and K_n at low α values.

The initial simulation phase established an isotropic stress state within the soil domain by enforcing a uniform vertical surcharging stress

($=100$ kPa for all FE analyses) at the top of soil domain and specifying $K_0 = 1.0$ to generate horizontal stress. The surcharging pressure reflects the embedment of the p-y module, although the FE results were independent of this choice, as the soil undrained strength and stiffness are independent of the confining stress, and no gap was able to form behind the ROBOCONE. Any soil deformation as a result of surcharging pressure was re-zeroed before activating the entire ROBOCONE system (i.e. CPT shaft, rings and p-y module). The horizontal loading of the p-y module was simulated in a displacement-controlled mode until the displacement reaches $10\%D_R$. The stack of rings was also assigned displacement-controlled movement with a linear variation with their individual vertical positions, giving a smooth transition between the moving p-y module and stationary CPT shaft. Note that the reaction forces considered in the subsequent interpretations were measured only on the ROBOCONE p-y module and not on the sliding rings, taking advantage of the ability to recover reaction forces at a reference point of a rigid body (PLAXIS, 2023).

4. Results: lateral bearing factors

In order to validate the numerical model, simulations were initially conducted for the p-y module with infinite height, i.e. plane strain conditions to eliminate end effects, allowing for a direct comparison with the upper bound solutions developed in Martin and Randolph (2006). Fig. 5 shows the variation with the normalised lateral reaction forces measured on the p-y module ($F_{t,RC}/(D_R H_R s_u)$) with the normalised lateral movements (u_{RC}/D_R), while the interface roughness factors (α) range from 0.01 to 1.0. Note that the minimum roughness factor of 0.01 was adopted in the present study to ensure the numerical stability, while in the previous semi-analytical upper bound analysis α was strictly set equal to be 0. All results indicate an initially linear behaviour followed by a plateau after a displacement of roughly between $2\% D_R$ and $4\% D_R$. The value of the plateau is used to calculate the lateral bearing factor of p-y module following the definition in Equations (2). A significant increase in bearing factors is anticipated with an increase in the roughness factor, consistent with the previous discussion in the upper limit analyses, though a negligible impact of roughness factor on the initial elastic stiffness is observed, a detail to be explored in subsequent discussions.

Fig. 6 compares bearing factors from the FE analysis with classical

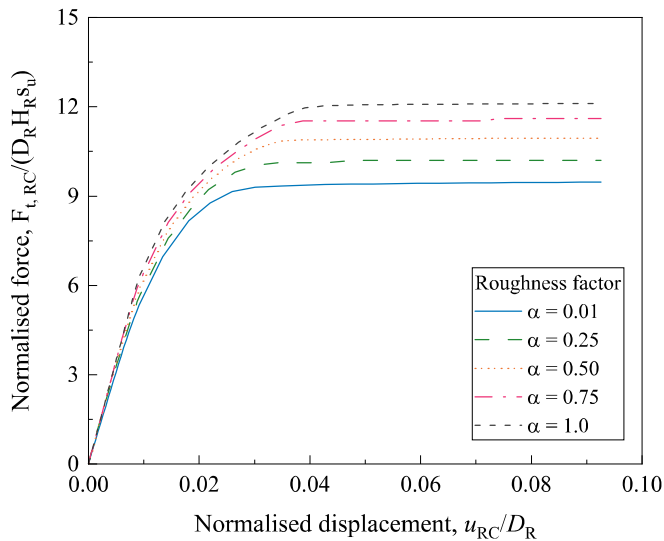


Fig. 5. Predicted behaviour of the plane strain p-y module with various interface roughness.

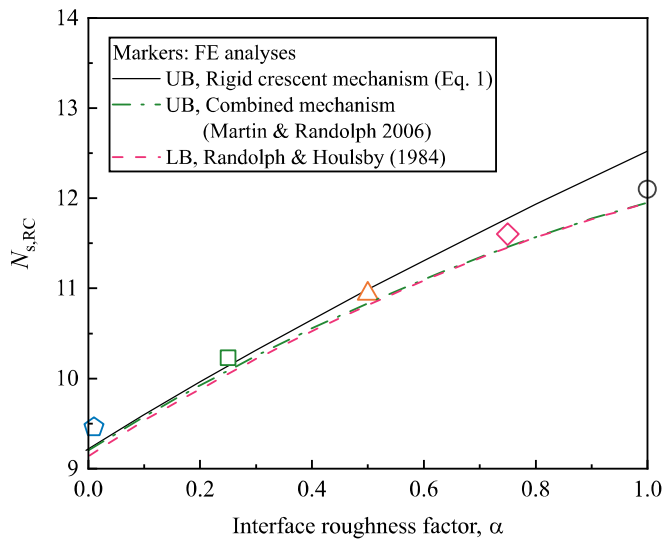


Fig. 6. Comparison between numerical shaft factor $N_{s,RC}$ shown by circular markers corresponding to interface roughness indicated in Fig. 5, and upper bound solutions (Martin and Randolph, 2006) shown by the line.

plasticity solutions of the bearing factors for infinitely long rigid piles, including the upper-bound solutions using the rigid crescent mechanism (Eq (1) and the combined mechanism (Martin & Randolph, 2006) and the lower-bound (LB) solutions by Randolph and Houlsby (1984). It is seen that FE analyses demonstrate an increase in the bearing factors by around 28% as the interface roughness varies from 0.01 to 1.0, while the numerical model slightly underestimates the bearing factors at $\alpha > 0.5$ compared to the upper bound solution from the rigid crescent mechanism. This discrepancy can be attributed to the fact that the rigid crescent mechanism by Martin & Randolph (2006) gives the most accurate results for the interfaces with small roughness factor. Moreover, FE bearing factors appear to be more consistent with the upper-bound solutions from the combined mechanism and the LB solutions of Randolph & Houlsby (1984) over the whole range of α , validating the robust reliability of the FE simulations in this study.

Fig. 7 presents a family of bearing factors for the finite length p-y module, characterised by the aspect ratio (H_R/D_R) and the interface roughness. This highlights the ‘end effect’ introduced and discussed in

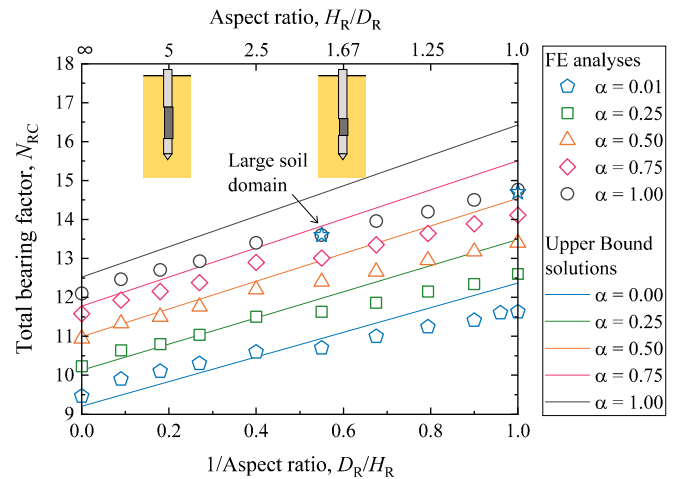


Fig. 7. Comparison of bearing factors between numerical and semi-analytical upper bound analyses.

the upper bound solution. Each marker in this figure represents a single FE simulation, while the continuous lines correspond to the upper bound solutions. It is clear that at a specific H_R/D_R , numerical bearing factors increase by 26%-28% with interface roughness factor increased from 0.01 to 1.0, similar to that for the infinite p-y module (see Fig. 5). Furthermore, at a specific interface roughness, the bearing factors indicate a nearly linear growth with inverse H_R/D_R , consistent with the developed semi-analytical solution in Equation (2), although they have different gradients. Two additional numerical models with larger soil domains ($\approx 148D_R$ diameter) produce nearly identical bearing factors, implying the size of soil domain adopted in Fig. 4 is sufficient to avoid any boundary effects. The discrepancy between the upper bound solution and the FE results ranges from 9.2% on average in plane strain conditions to 39.1% at the lowest aspect ratio ($=1.0$). A closer analysis of the failure mechanism from the FE simulation can inform this discrepancy, as discussed later.

Fig. 8 shows contours of relative shear stress (τ_{rel}) near a representative p-y module ($H_R/D_R = 4.0$, $\alpha = 0.8$) at a lateral movement of 4% D_R , where ultimate capacity is considered to be fully mobilised (i.e. at the plastic plateau, see Fig. 5). Note that the relative shear stress (τ_{rel}) is defined as the ratio of the mobilised shear stress to the undrained shear strength (s_u), which offers an indication of the proximity of the stress point to the failure envelope. As seen in Fig. 8 (a), a clear failure zone ($\tau_{rel} = 1.0$) symmetry to the CPT longitudinal is identified, which can roughly be identified into a cylindrical volume (Zone I) and a cap zone (Zone II) extending above the p-y module. The same mechanisms were observed in other simulations with different H_R/D_R ratios and interface roughness. This might explain partially the difference in bearing factor between numerical and semi-analytical analyses as shown in Fig. 7, as the upper bound solution assumes soil failure only occurs right in front of and behind the p-y module. It is interesting to note that the area of the plastic failure Zone II is similar for p-y modules with different H_R/D_R ratios at the same lateral movements, which will be marked by a similar displacement field in this zone, as discussed subsequently. Fig. 8 (b) and (c) show the distribution of relative shear stress across two representative horizontal cross sections. As seen in Cross section A-A, a nearly axisymmetric failure zone took place within the soil domain as the p-y module moves laterally, leading to a high deviatoric stress area in that zone. However, the failure area ($\tau_{rel} = 1.0$) along the cross-section B-B is not axisymmetric; instead, a relatively thin failure zone is observed in the direction normal to the p-y module movements, where the soil was considered to be less disturbed.

Successful development of an upper bound plasticity solutions relies on the accuracy of the postulated soil failure mechanism (Randolph and Houlsby, 1984). To compare the postulated and simulated mechanisms,

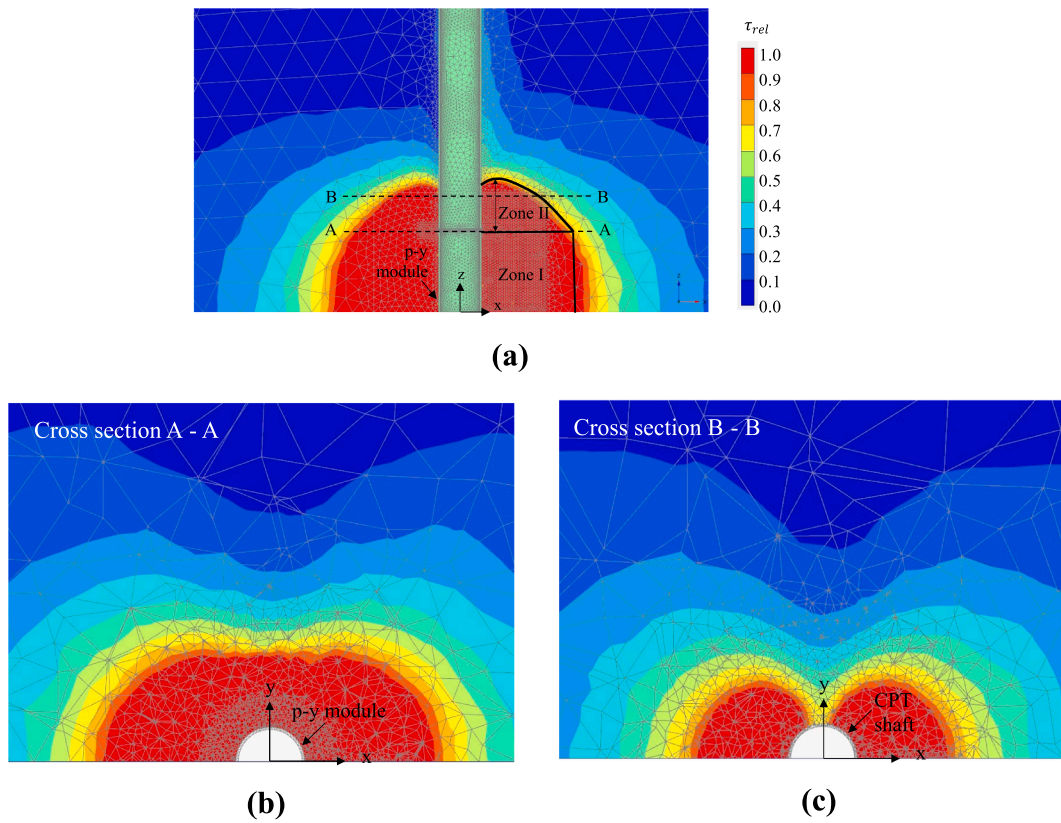


Fig. 8. Contours of the relative shear stress field near the p-y module moving along x axis: (a) longitudinal cross section; (b) lateral cross section (A-A) at the level of p-y module end; (c) lateral cross section (B-B) at the level of $1.0 D_R$ from the p-y module end.

the upper bound analysis was compared with the field of incremental plastic displacement at the end of the FE analysis along the cross-section A-A, which represent the soil velocity at points along the failure mechanism. Fig. 9 shows the incremental displacement field interpolated from the FE results along a series of streamlines that were centred at O and defined by the actual λ values for the given H_R/D_R ratios and α (see Fig. 3a). These streamlines fall within the soil failure zone identified in the Fig. 8 where the plastic deformation occurs. The vectors of incremental plastic displacement are generally tangential to these streamlines, consistent with the assumption in Fig. 2, while the main exceptions can be found in the region directly in front of and behind the p-y module, where the soil primarily shifts in the x-direction with the p-y module in FE simulations. Also, the vector lengths, indicative of the magnitudes of incremental plastic displacements, are more uniformly distributed across these streamlines in the case with $\alpha = 0.01$ than that with $\alpha = 1.0$. This observation aligns with the previous postulation in Martin & Randolph (2006) that the soil failure pattern adopted in the present study is more consistent with smooth interface, which also caused an increasing discrepancy in the bearing factor when interface becomes rough.

While the previous upper bound solution considered a two-dimensional soil failure mechanism at the end plane of the p-y module, the numerical analysis reveals an apparent three-dimensional deformation pattern in that region. Fig. 10 (a) illustrates the variation of soil vertical displacement with the normalised radial distance from the shaft at the elevation of the p-y module end plane. The vertical displacement is normalised by the current horizontal movement of the p-y module (in this case $u_{RC} = 5$ mm). It is clear that the normalised displacement in the front of the moveable part increases sharply to around 0.25 followed by an abrupt drop prior to stabilising towards zero at far radial distances ($\approx 6R$). A similar pattern of the soil vertical displacement is observed behind the p-y module, although moving downwards. The displacement profiles remain essentially constant

irrespective of aspect ratios, consistent with the previous statement that the failure Zone II (see Fig. 8) has similar characteristics regardless of the H_R/D_R ratios. The impact of the interface roughness is also explored through considering the same displacements with an interface roughness $\alpha = 0.01$, while no evident effect is identified as seen in Fig. 10 (b). Fig. 10 (c) shows the evolution of vertical displacement at six points that are symmetrical to the vertical axis of the p-y module against the current p-y module lateral movement. As expected, the trends of these curves are symmetrical in front of and behind p-y module and they initially behave linearly prior to the plastic yielding. Though soil elements at far distance from shaft seem eventually to reach a plateau, at the closest points their vertical displacement keeps increasing with the lateral movement of p-y module.

A mechanism-based model, depending on α and H_R/D_R ratios and validated against the FE results was developed to facilitate a practical design process. The numerically calculated bearing factor (N_{RC}) was normalised by the numerical plane strain bearing factor ($N_{s,RC}$). Fig. 11 shows that the normalised $N_{RC}/N_{s,RC}$ describes a linear relationship if plotted against the aspect ratio, irrespective of the interface roughness. This trend, implying an end bearing factor approximately 23% of the shaft bearing factor in plane strain conditions, can be reflected by the empirical Equation (14), with the coefficient of determination (R^2) of 0.97. The employment of numerical bearing factor in plane strain conditions (see Fig. 6) and Eq. (14) facilitate to produce the bearing factor graph, as shown in Fig. 12, which indicates a reasonable match to FE results.

$$N_{RC} = \left[1 + \left(\frac{N_{e,RC}}{N_{s,RC}} \right) \left(\frac{D_R}{H_R} \right) \right] N_{s,RC} = \left[1 + 0.23 \left(\frac{D_R}{H_R} \right) \right] N_{s,RC} \quad (14)$$

5. Results: elastic stiffness factors

Fig. 13 shows the illustrative load displacement response of a typical

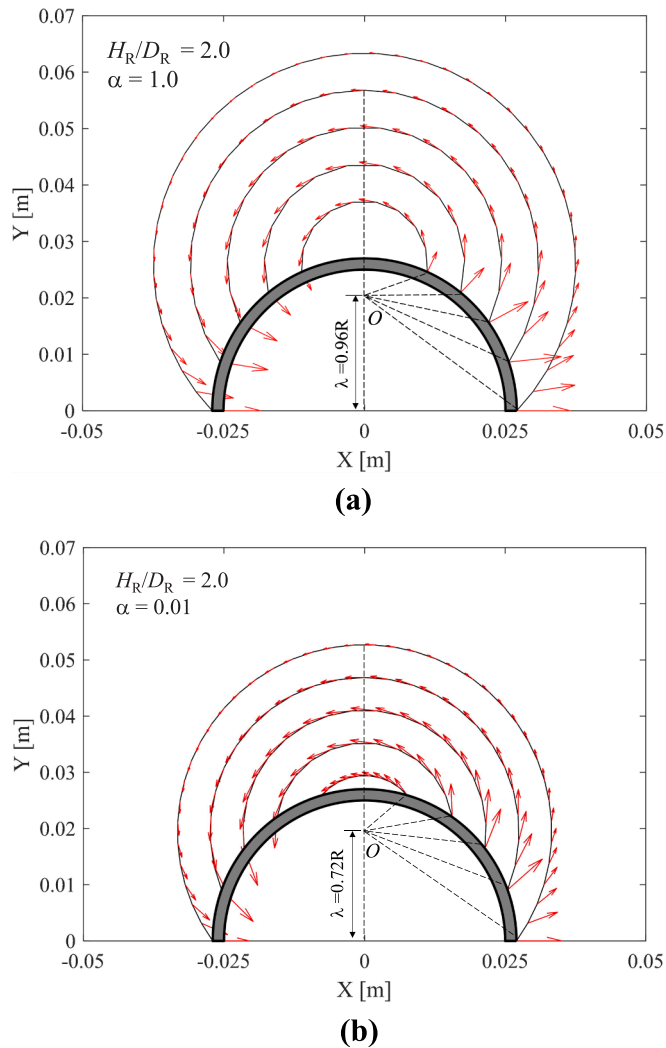


Fig. 9. Incremental plastic strain at the end plane along the streamlines assumed in the upper bound analyses: (a) rough interface with $\alpha = 1.0$; (b) quasi-smooth interface with $\alpha = 0.01$.

p-y module, where the reaction force ($F_{t,RC}$) is normalised by the product of the length and diameter of the p-y module ($H_R D_R$) and the lateral movement (u_{RC}) is normalised by the p-y module diameter (i.e. u_{RC}/D_R). The initial slope of the p-y module load–displacement response can be related to the elastic shear modulus (G) of the material, which behaves elastically at small strain. The secant stiffness is plotted on a logarithmic scale as a function of normalised lateral displacement (u_{RC}/D_R) to highlight the small-scale behaviour of the module, where the maximum secant stiffness at small displacement can be linked to elastic shear module through the use of elastic stiffness factor (k_{RC}).

Fig. 14 (a) shows the influence of interface roughness on the evolution of normalised secant stiffness against the lateral module movement (u_{RC}/D_R) of a p-y module, while adopting $H_R/D_R = 1.0$ and default interface stiffness of $K_{s,i} = 4.7 \text{ E5 kN/m}^3$ and $K_{n,i} = 5.17 \text{ E6 kN/m}^3$. The stiffness factor K_{RC} is defined as the plateau in normalised stiffness at very small displacements. It is observed that interface roughness α has a marginal effect on the K_{RC} at initial loading, though it does influence the degradation of the normalised secant stiffness. This is due to the fact that α only controls the interface strength and transition from sticking to slipping states. At very small displacements, the interface is still “elastic” (sticking phase), hence α has no influence.

Fig. 14 (b) shows that increasing interface stiffness (K_s and K_n) enhances the normalised secant stiffness and stiffness factor (K_{RC}). This is

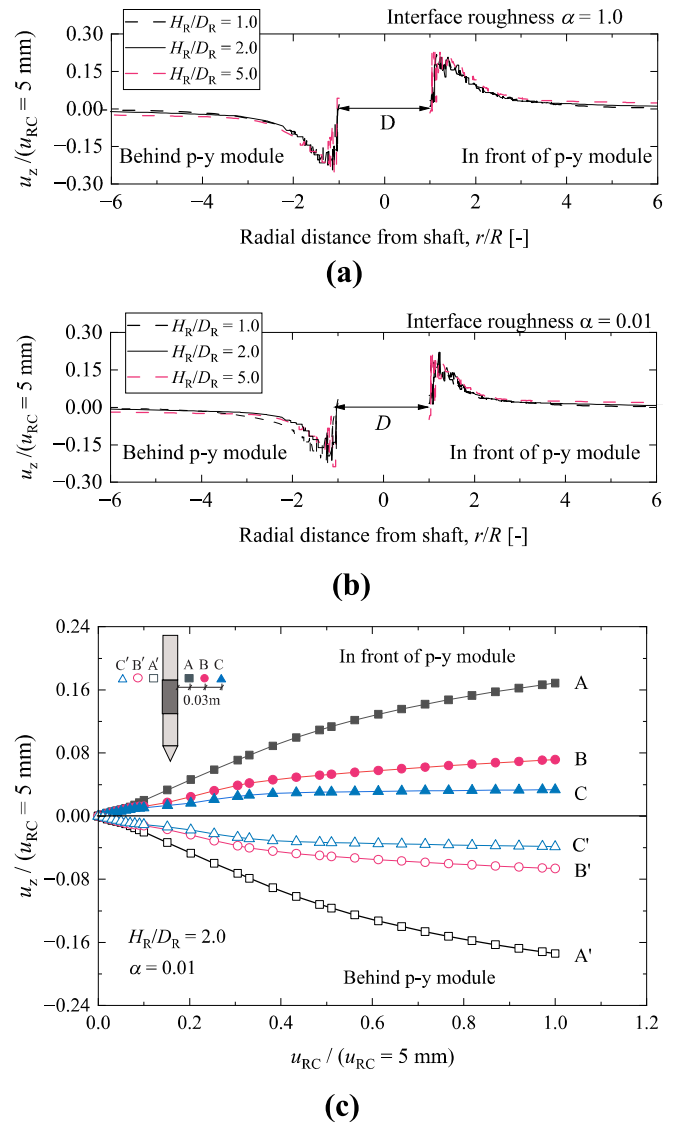


Fig. 10. (a) Profiles of soil vertical displacement at the end plane ($\alpha = 0.01$); (b) Profiles of soil vertical displacement at the end plane ($\alpha = 1.0$); (c) Evolution of vertical movement at representative soil elements throughout the horizontal translation of p-y module.

due to the penalty approach to simulate the zero-thickness interface behaviour, which induces additional compliance due to the interpenetration of the structural and soil meshes (Cerfontaine et al., 2015). Increasing the normal stiffness (K_n) reduces this interpenetration, which is more realistic. Results indicate that the initial stiffness factors seem to converge to a certain value when employing larger K_s and K_n values.

Fig. 14 (c) shows the considerable influence of the aspect ratio H_R/D_R on the stiffness factor K_{RC} , while adopting the default interface stiffness and $\alpha = 1.0$. The lower the H_R/D_R , the markedly stiffer the initial response, indicating the important role of end effects in the shorter p-y module. These sensitivity analyses serve a basis for producing a stiffness factor graph similar to that for the bearing factor (see Fig. 12).

Fig. 15 summarises the stiffness factors corresponding to different p-y module aspect ratio H_R/D_R ranging from infinity to unity. Each marker represents a single FE simulation. It is clear that the stiffness factor increases with the inverse of the H_R/D_R ratio. Moreover, for p-y module with H_R/D_R near infinity, the stiffness factors fall generally within the range of 4.0 and 6.0, which are aligned with the estimations ranging from 4.5 to 7.0 for piles in clays and sands (Jeanjean, 2009; Burd et al., 2020), although they markedly exceed the analytical ‘stiffness factor’ of

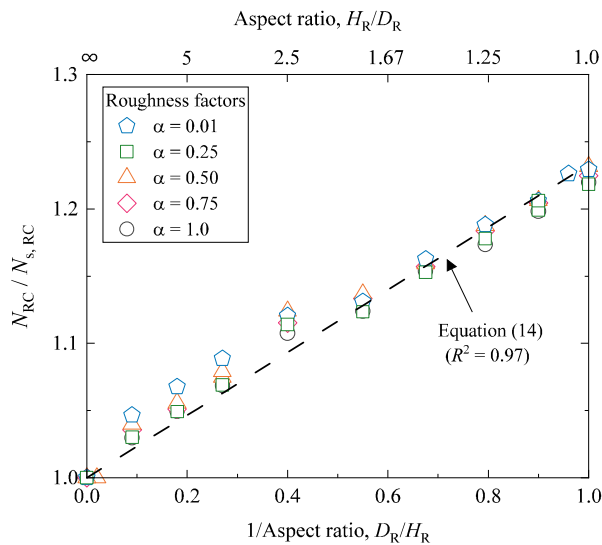


Fig. 11. Normalised bearing factor $N_{RC}/N_{s,RC}$ and the approximating expression in Eq. (14).

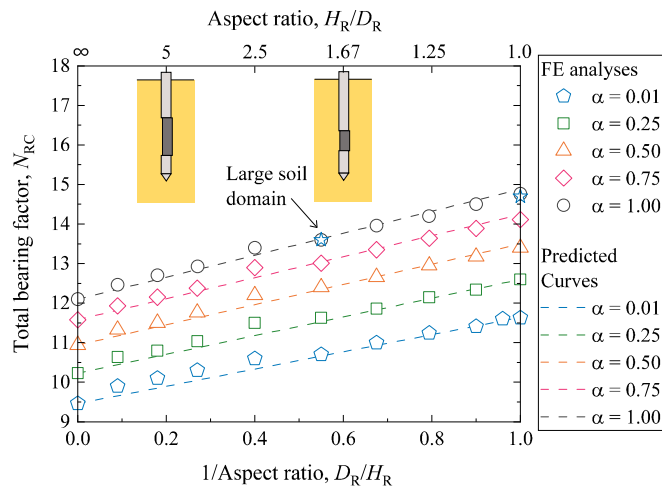


Fig. 12. Predicted lateral bearing factors by Eq. (14) compared to numerical FE results.

2.0 for pressuremeter tests in undrained soils (Houlsby and Carter, 1993).

An approximately threefold enhancement in stiffness factor K_{RC} is evident as aspect ratio H_R/D_R transitions from infinity to unity, in contrast to the modest 21–23% increment observed for bearing factors with varying H_R/D_R (see Fig. 7). Furthermore, unlike the roughly linear growth in bearing factor with aspect ratio, the influence of H_R/D_R on the K_{RC} appears to stabilise when H_R/D_R is higher than 10.0. Results from two additional numerical models with larger soil domains ($\approx 148D_R$ in diameter) are marked in Fig. 12. These produce identical stiffness factors, indicating again that the soil domain adopted in this study is sufficiently large to avoid any boundary effects. Also plotted in Fig. 15 is the impact of the interface stiffness on K_{RC} , where both K_s and K_n are increased by 20, 40 and 80 times the initially default $K_{s,i}$ ($=4.7 \text{ E5 kN/m}^3$) and $K_{n,i}$ ($=5.17 \text{ E6 kN/m}^3$), respectively. Of interest is that the influence of interface stiffness varies with aspect ratio, converging to certain values when substantially higher K_s and K_n are adopted. For example, for p-y module with infinite aspect ratio, marginal influence of interface stiffness is observed for a p-y module with an infinite aspect ratio, while at $H_R/D_R = 1.0$, the stiffness factor seems to converge to around 16.7 from 12. As with bearing factor, it is useful to propose an

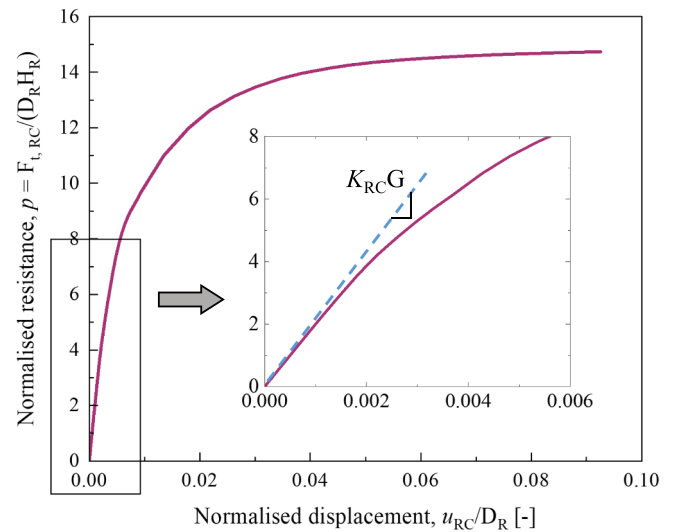


Fig. 13. Typical p-y module load-displacement response for interpretation of stiffness factor (K_{RC}).

empirical formulation to stiffness factor graphs generated by these FE analyses to allow results to be generalised in practical design. Expressed by Equation (15) with a cut-off value of 5.0, it is able to provide an approximate upper limit to the numerical stiffness factors, where the influence of interface stiffness is mitigated by constraining relative interface shear and normal displacement to a minimum.

$$K_{RC} \approx 4.13 + 12.5 \left(\frac{D_R}{H_R} \right)^{0.8} \geq 5.0 \quad (15)$$

6. Discussion on the optimum geometry of p-y module

The mechanism-based empirical models developed from the above FE results offer a basis for the interpretation of p-y module measurements with any geometry (i.e. H_R/D_R) in undrained clay, through the quick determination of lateral bearing factors and stiffness factors. For practical design of a p-y module, a specific H_R/D_R must be selected. The initial prototype p-y module has a diameter of 54 mm, consistent with a 15 cm² cone penetrometer, which is sufficient to house the components of the internal mechanism, miniature sensors and cables (Creasey et al., 2023). The longer the p-y module, the weaker the end effects but the greater the actuation force required to displace the p-y module and bring the clay to failure. Conversely, the shorter the p-y module, the stronger the end effects but the lower the actuation force required. Based on the above FE results, the optimal aspect ratios (H_R/D_R) of a practical p-y module are suggested to range from 1.5 to 5.0, as a balance between minimizing the end effects and ensuring the mechanical feasibility.

A p-y module prototype with a H_R/D_R of 3.7 ($H_R = 200 \text{ mm}$) is currently being trialled (Creasey et al., 2023), whose measurement in undrained clay requires a stiffness factor (K_{RC}) of 8.52 and bearing factors (N_{RC}) ranging from 10.26 to 12.9 depending on the interface roughness (varying from 0 to 1.0), according to the interpretation framework proposed. In this case, the ‘end effect’ contributes to around 5–7% of the total bearing factors, which is a relatively lower magnitude from an engineering perspective. Consequently, if this prototype is embedded in soft or stiff clays with typical undrained shear strengths ranging from 5 kPa to 300 kPa (De Vallejo & Ferrer, 2011), it will require a pushing force of 0.5–33.2 kN to displace the p-y module and bring the clay to failure. This type of calculation aids the mechanical design of the ROBOCONE actuation system. For the p-y module with other geometries, same procedures can be deployed to estimating the mechanical pushing forces and thus aid the design of ROBOCONE system.

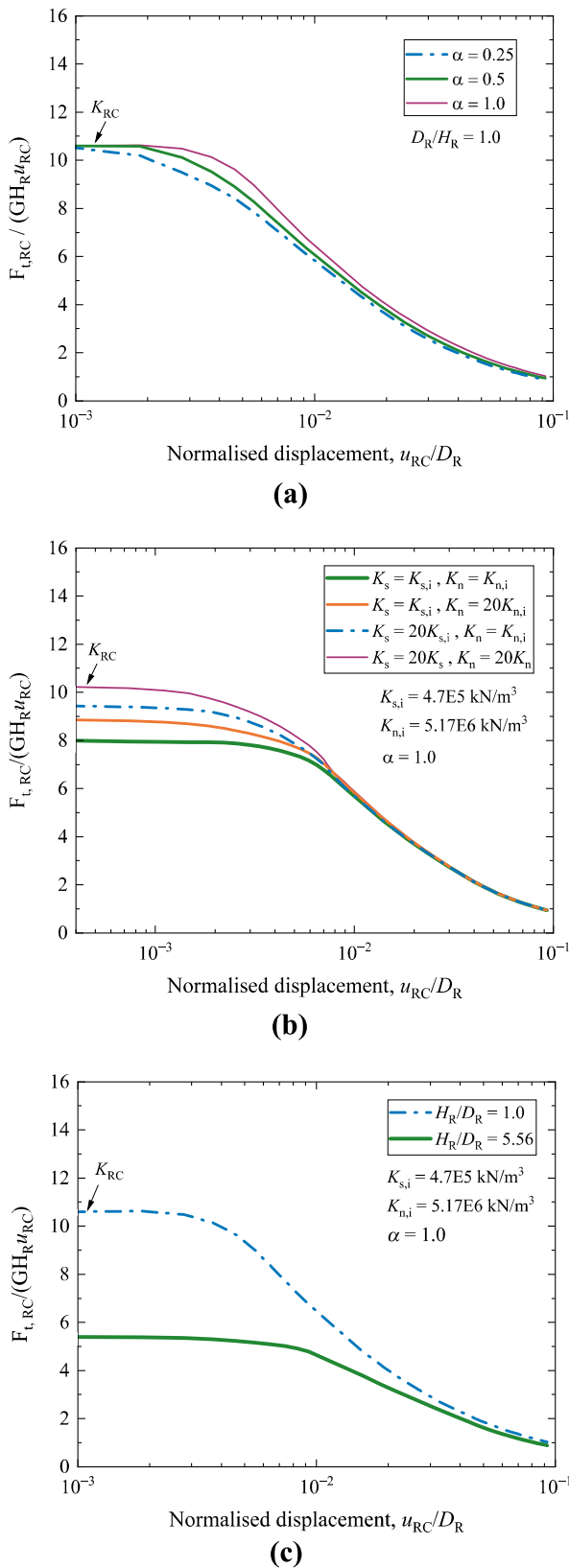


Fig. 14. Sensitivity of stiffness factor to (a) interface roughness α ; (b) interface stiffness parameters K_s and K_n ; (c) aspect ratio, H_R/D_R .

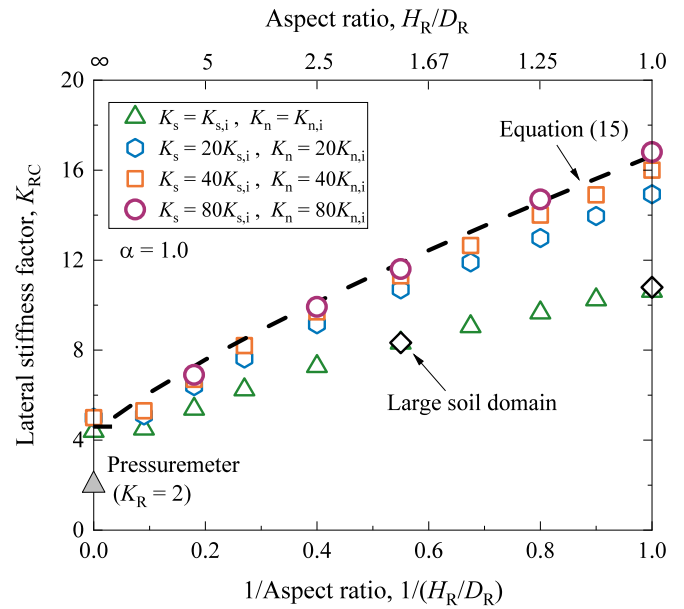


Fig. 15. Stiffness factor variation with aspect ratio, interface stiffness and roughness.

7. Conclusions

A novel robotic ground characterisation tool is developed by implementing a cylindrical section of cone capable of horizontal translation within an augment CPT shaft, namely ROBOCONE p-y module. The goal of this paper is to provide guidance for linking the direct measurements of a p-y module to key ground geotechnical parameters (i. e. undrained shear strength, elastic shear modulus) through semi-analytical upper-bound analyses and three-dimensional finite element simulations. The systematic exploration considered the effects of interface roughness, interface stiffness, and the aspect ratio of the p-y module on bearing factor (N_{RC}) and stiffness factor (K_{RC}). The following conclusions can be reached from the present study.

- (1) Based on the semi-analytical upper bound analyses, the bearing factors of the p-y module increases with the interface roughness and the inverse aspect ratio (D_R/H_R) due to the end effects. It increases by 34% from $D_R/H_R = 0$ to $D_R/H_R = 1$, ranging from 9.2 to 16.4.
- (2) Reasonable match between the FE analyses of the infinitely long p-y modules in plane strain and semi-analytical upper bound bearing factor solutions by Martin and Randolph (2006) proves the validity of the adopted FE model.
- (3) The FE analyses of the finite length p-y module capture the three-dimensional soil failure mechanism during the horizontal translation of p-y module. Two failure zones above and below the upper and lower end plane of the p-y module are related to the soil vertical movement in that region, deviating from the plane strain conditions. Numerical bearing factors of p-y module indicate a nearly linear growth with the inverse aspect ratio, with a gradient of 21–23% at various interface roughness. Based on the FE simulations, a mechanism-based empirical formulation is proposed to estimate the bearing factors, and enables a quick interpretation of the soil undrained strength from the ROBOCONE results.
- (4) A simple approximating expression, validated against FE simulations, was proposed to capture variation of the small-displacement elastic stiffness factors (K_{RC}) as a function of the aspect ratio (H_R/D_R). While the interface roughness has negligible influence on the stiffness factors, the interface stiffness is

found to play a significant role in the determination of elastic shear modulus. The relationship comprises an upper bound curve where the interface stiffness effect is eliminated and a minimal cut-off value of 5.0 for the aspect ratio close to infinity.

Overall, the FE and the upper bound analyses in the present study not only contribute to optimizing the design of ROBOCONE p-y module but also aid engineers in understanding how the small-displacement elastic stiffness and ultimate bearing capacity of a p-y module within a ROBOCONE protocol can be used to determine undrained shear strength and elastic shear modulus of soil associated with a linearly elastic perfectly plastic constitutive model. Further analyses are needed to investigate the responses of p-y module subjected to undrained cyclic horizontal loading, in which case a more advanced soil constitutive module needs to be adopted.

CRedit authorship contribution statement

Kai Wen: Writing – original draft, Methodology, Investigation, Conceptualization. **Benjamin Cerfontaine:** Writing – review & editing, Supervision, Methodology, Funding acquisition. **David White:** Writing – review & editing, Supervision, Methodology, Investigation, Funding acquisition. **Susan Gourvenec:** Writing – review & editing, Supervision, Methodology, Investigation, Funding acquisition. **Andrea Diambra:** Writing – review & editing, Supervision, Methodology, Investigation, Funding acquisition.

Declaration of competing interest

The authors declare that they have no known competing financial interests or personal relationships that could have appeared to influence the work reported in this paper.

Data availability

Data will be made available on request.

Acknowledgements

The authors would like to acknowledge the financial support from the Engineering and Physical Sciences Research Council (EPSRC - Ref: EP/W006235/1) and Science Foundation Ireland (SFI - Ref: 21/ EPSRC/ 3787). Susan Gourvenec is supported through the Royal Academy of Engineering Chair in Emerging Technologies Scheme. David White is also supported through the EPSRC Offshore Renewable Energy Supergen Hub (EPSRC – Ref: EP/Y016297/1).

References

Bateman, A.H., Mylonakis, G., Creasey, J., El Hajjar, A., White, D., Cerfontaine, B., Gourvenec, S., Andrea, D., 2023. p-y curves from in-situ ROBOCONE tests: a similarity approach for laterally loaded piles in clay. *Symposium on Energy Geotechnics* 2023, 1–2. <https://doi.org/10.59490/seg.2023.607>.

- Burd, H.J., Taborda, D.M., Zdravković, L., Abadie, C.N., Byrne, B.W., Houlsby, G.T., et al., 2020. PISA design model for monopiles for offshore wind turbines: application to a marine sand. *Geotechnique* 70 (11), 1048–1066.
- Byrne, B.W., Houlsby, G.T., Burd, H.J., Gavin, K.G., Igoe, D.J., Jardine, R.J., et al., 2020. PISA design model for monopiles for offshore wind turbines: application to a stiff glacial clay till. *Geotechnique* 70 (11), 1030–1047.
- Cerfontaine, B., Dieudonné, A.C., Radu, J.P., Collin, F., Charlier, R., 2015. 3D zero-thickness coupled interface finite element: Formulation and application. *Comput. Geotech.* 69, 124–140.
- Cerfontaine, B., White, D., Kwa, K., Gourvenec, S., Knappett, J., Brown, M., 2023. Anchor geotechnics for floating offshore wind: Current technologies and future innovations. *Ocean Eng.* 279, 114327.
- Charles, M., Yu, H. S., & Sheng, D. (2020). Finite element analysis of pressuremeter tests using critical state soil models. In *Numerical Models in Geomechanics* (pp. 645-650). CRC Press.
- Creasey, J., Hajjar, A.E., Conn, A.T., Ibraim, E., Bateman, A.H., Mylonakis, G., Martin, G., Diambra, A., Cerfontaine, B., Gourvenec, S., White, D.J., Igoe, D., Kasyap, S., 2023. In: *Motivation and demonstration of robotic tolling for ground characterisation: the ROBOCONE*. Society of Underwater Technology, London, UK, pp. 368–375.
- De Vallejo, L.G., Ferrer, M., 2011. *Geological engineering*. CRC Press.
- Diambra, A., Creasey, J., Leonet, J., Conn, A., Ibraim, E., Mylonakis, G., White, D., Cerfontaine, B., Gourvenec, S., & Igoe, D. (2022). Concept design of a new CPT module for direct in situ measurement of py soil responses. In *Cone Penetration Testing 2022* (pp. 900-906). CRC Press.
- Houlsby, G.T., Carter, J.P., 1993. The effects of pressuremeter geometry on the results of tests in clay. *Geotechnique* 43 (4), 567–576.
- Jeanjean, P., A. Zakeri, Y. Zhang, and K. H. Andersen. (2022). The new ISO/ APY p-y curves in clays and their reconciliation with the PISA framework. In: *Proc., of the Offshore Technology Conf., OTC-31860-MS*. Houston, TX: Offshore Technology Conference (OTC), ss.
- Jeanjean, P. (2009). Re-assessment of p-y curves for soft clays from centrifuge testing and finite element modeling. In *Proceeding of Offshore technology conference*, 1–23. Houston: Offshore Technology Conference.
- Liu, J., Chen, X., Han, C., Wang, X., 2019. Estimation of intact undrained shear strength of clay using full-flow penetrometers. *Comput. Geotech.* 115, 103161.
- Martin, C.M., Randolph, M.F., 2006. Upper-bound analysis of lateral pile capacity in cohesive soil. *Geotechnique* 56 (2), 141–145.
- Martinez, A., Frost, J.D., 2018. Undrained behavior of sand–structure interfaces subjected to cyclic torsional shearing. *J. Geotech. Geoenviron. Eng.* 144 (9), 04018063.
- Matlock, H. (1970). Correlations for design of laterally loaded piles in soft clay. In: *Proceedings of the 2nd Annual Offshore Technology Conference*, Dallas. OTC-1204. pp. 577–594.
- Moavenian, M.H., Nazem, M., Carter, J.P., Randolph, M.F., 2016. Numerical analysis of penetrometers free-falling into soil with shear strength increasing linearly with depth. *Comput. Geotech.* 72, 57–66.
- PLAXIS (2023). *PLAXIS 3D Reference Manual*. PLAXIS, Delft, the Netherlands.
- Randolph, M. F., Hefer, P. A., Geise, J. M., & Watson, P. G. (1998). Improved seabed strength profiling using T-bar penetrometer. *Int. Conf. Offshore Site Investigation and Foundation Behaviour*. SUT, London. pp. 221-235.
- Randolph, M.F., Houlsby, G.T., 1984. The limiting pressure on a circular pile loaded laterally in cohesive soil. *Geotechnique* 34 (4), 613–623.
- Teh, C.I., Houlsby, G.T., 1991. An analytical study of the cone penetration test in clay. *Geotechnique* 41 (1), 17–34.
- Truong, P., & Lehane, B. (2014). Numerically derived CPT-based py curves for a soft clay modeled as an elastic perfectly plastic material. In *3rd Int. Symp. on Cone Penetration Testing* (pp. 975-982).
- White, D.J., 2022. CPT equipment: Recent advances and future perspectives. *Cone Penetration Testing* 2022, 66–80.
- White, D.J., Doherty, J.P., Guevara, M., Watson, P.G., 2022. A cyclic py model for the whole-life response of piles in soft clay. *Comput. Geotech.* 141, 104519.
- Yan, Y., White, D.J., Randolph, M.F., 2011. Penetration resistance and stiffness factors for hemispherical and toroidal penetrometers in uniform clay. *Int. J. Geomech.* 11 (4), 263–275.
- Yu, H.S., Charles, M.T., Khong, C.D., 2005. Analysis of pressuremeter geometry effects in clay using critical state models. *Int. J. Numer. Anal. Meth. Geomech.* 29 (8), 845–859.